High-Performance Lithium-Ion Battery and Symmetric Supercapacitors Based on FeCo$_2$O$_4$ Nanoflakes Electrodes

Saad Gomaa Mohamed,[†,‡] Chih-Jung Chen,[†] Chih Kai Chen,[†] Shu-Fen Hu,*[,§] and Ru-Shi Liu*[,†,⊥]

[†]Department of Chemistry, National Taiwan University, Taipei 106, Taiwan

[‡]Nanoscience and Technology Program, Taiwan International Graduate Program, Institute of Physics, Academia Sinica and National Taiwan University, Taipei 106, Taiwan

[§]Department of Physics, National Taiwan Normal University, Taipei 116, Taiwan

[⊥]Department of Mechanical Engineering and Graduate Institute of Manufacturing Technology, National Taipei University of Technology, Taipei 106, Taiwan

S *Supporting Information*

ABSTRACT: A successive preparation of FeCo$_2$O$_4$ nanoflakes arrays on nickel foam substrates is achieved by a simple hydrothermal synthesis method. After 170 cycles, a high capacity of 905 mAh g^{-1} at 200 mA g^{-1} current density and very good rate capabilities are obtained for lithium-ion battery because of the 2D porous structures of the nanoflakes arrays. The distinctive structural features provide the battery with excellent electrochemical performance. The symmetric supercapacitor on nonaqueous electrolyte demonstrates high specific capacitance of 433 F g^{-1} at 0.1 A g^{-1} and 16.7 F g^{-1} at high scan rate of 5 V s^{-1} and excellent cyclic performance of 2500 cycles of charge−discharge cycling at 2 A g^{-1} current density, revealing excellent long-term cyclability of the electrode even under rapid charge−discharge conditions.

KEYWORDS: *FeCo$_2$O$_4$, nanoflakes, Li-ion battery, supercapacitors*
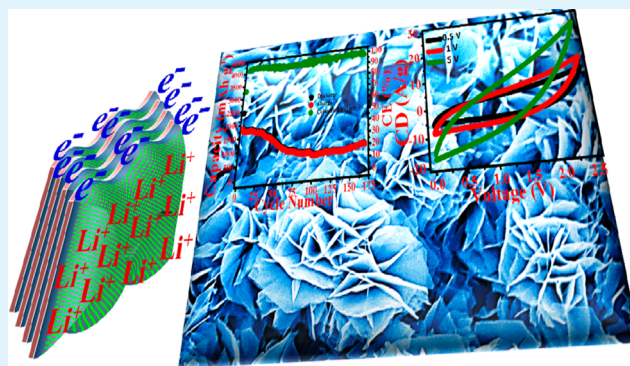
1. INTRODUCTION

Lithium-ion batteries (LIBs) and supercapacitors (SCs) have enticed worldwide interest as two main devices of electric energy storage on account of their needful use as predominant energy sources for transportable electronics and their prominent prospect to electric vehicles and large-scale electric networks.[1] Both of them are categorized as electrochemical energy storing systems and have numerous resemblances in structure with an anode, an utilized electrolyte, and a cathode.[2] Fundamentally, the storing of energy in those electrochemical cells is based on the reversible electrochemical reactions and the mechanism of charge storing in the electrode materials. The ions travel toward the electrodes across the electrolytes, whereas the electrons flow over the outer circuit during the electrochemical processes.[1]

In consequence of their outstanding physical and chemical properties and considerable prospective for several applications in technological fields, mixed transition metal oxides (MTMOs) have lately enticed research interest, extending from material for electrodes to catalysts. MTMOs normally store lithium through conversion reaction in case of using as anode materials for LIBs, which causes the reversible formation of metallic particles implanted in a Li$_2$O matrix.[1,3,4] In case of using as electrode for SCs, the storing of charges in MTMO

electrodes primarily originates from the pseudocapacitance that initiates from the fast surface redox reactions.[1,5] Aside from simple binary metal oxides, ternary transition metal oxides have drawn growing attention for electrochemical energy storage in recent years. They show many unique properties that originate from the coexistence of two different cations in a single crystal structure,[6] as well as partial replacement of M in spinel M$_3$O$_4$ with other 3d-transition metals (Mn, Fe, Co, or Ni) that can enhance the catalytic activity, selectivity, stabilization, and oxides withstanding against the catalytic or electrocatalytic poisoning.[7] For example, ternary MnCo$_2$O$_4$, NiCo$_2$O$_4$, CuCo$_2$O$_4$, and ZnCo$_2$O$_4$ have been widely reviewed as promising electrodes for LIBs and SCs because of their higher conductivity and electrochemical activities in comparison with corresponding M$_x$O$_y$ and Co$_3$O$_4$.[8−14] Furthermore, cobalt based oxides are to some extent expensive and toxic. Hence, beneficial attempts have been exerted toward partly displacing the cobalt in Co$_3$O$_4$ with cheaper and more environmentally friendly alternate elements without losing its high electrochemical effectiveness.[1]

Recently, the two-dimensional (2D) nanostructures, such as graphene, metal oxides, metal, chalcogenides, and hydroxides, have attracted tremendous attention because of their attractive physical and chemical properties for great potential applications in in catalysis and energy devices. Nanosheets have a large surface area, which provides high efficient electrochemical active sites, reduces the ions and electron diffusion path, increases the electronic conductivity, and improves the structural stability. Thus, the ultrathin 2D nanostructures represent a great potential for application in next generation batteries and supercapacitors.[15,16]

Very few studies have been reported on the utilization of $FeCo_2O_4$ as electrode material for energy-related applications. Laouini et al.[17] investigated the electrochemical behavior and the catalytic activity for oxygen evolution and reduction of $FeCo_2O_4$ thin film coatings. Sharma et al.[18] studied the electrochemical lithium storage properties of $FeCo_2O_4$ powder (submicron particles) and concluded that the iron ion is active alongside the cobalt ion. Their findings exhibited that Fe is more proper matrix ion than Mg, and $FeCo_2O_4$ showed the first discharge capacity of 1155 mAh g^{-1} and retained 90% of the first charging capacity of 827 mAh g^{-1} after 50 cycles at a current density of 60 mA g^{-1}. These results reveal the potential and possible use of $FeCo_2O_4$ as LIB electrode. No study regarding the application of $FeCo_2O_4$ as an electrode for SC application has been reported.

In this work, $FeCo_2O_4$ nanoflakes (FCO-NFs) were directly grown onto nickel substrate (free from adding binder or conductivity agent) through urea combustion hydrothermal synthesis then calcing for 2 h at 400 °C. To the best of our knowledge, this work is the first to examine the functioning of FCO-NFs as LIBs and SCs electrode system. Compared with three-electrode structure, measurement by means of two-electrode shape is more suitable for estimating the operation of SC test cells because they simulate the physical configuration, interior voltages, and charging transference in existent SC uses, accordingly providing the best evaluation of the rendering of such electrode materials.[19] on the contrary, the working electrode of a three-electrode cell has twice the potential range applied as is applied to the electrodes in a two electrode cell and this results in a doubling of the calculated capacitance, besides, the heightened sensitivity of the three electrode configuration can lead to large errors when projecting the energy storage capability of an electrode material for subercapacitors use.[20] Therefore, we fabricated our SC cell using two-electrode configuration (symmetric SC) in organic electrolyte. We investigated the electrochemical energy storage of FCO-NFs as electrodes both in LIBs and in SCs. As anode materials for LIBs, the electrode displays high first discharge capacity and maintain a high reversible capacity of 905 mAh g^{-1} at 200 mA g^{-1} rate after 170 cycles. When evaluated as SC electrode, they demonstrate high capacitance and good cycling constancy at high rates and high charge−discharge stability for 2500 cycles. These outstanding results indicate that the unique 2D-arrayed FCO-NFs structures on nickel foam are promising in electrochemical energy storage purposes.

2. EXPERIMENTAL SECTION

2.1. Hydrothermal Synthesis of FCO-NFs. $FeCo_2O_4$ prepared by dissolving a proper weight 1 mmol ferrous chloride tetrahydrate [$FeCl_2 \cdot 4H_2O$, 99%, J. T. Baker], 2 mmol cobalt nitrate hexahydrate [$Co(NO_3)_2 \cdot 6H_2O$, 99%, ACROS], 5 mmol urea [$CO(NH_2)_2$, 99%, Sigma-Aldrich], and 2 mmol ammonium fluoride (NH_4F, 98%,

Merck) in 50 mL of deionized water (DIW). Nickel foam substrate (2 cm × 3 cm piece, Kunshan Desike Electronic, China) was ultrasonically cleaned with ethanol, DIW, and acetone (30 min of successive sonication in each). The solution with the nickel foam (top side was masked by kapton tape) kept on top was next transmitted directly into a 100 mL Teflon-lined stainless autoclave that then was sealed and kept for 7 h at 140 °C. After the autoclave was left to cool down naturally to room temperature, the as-synthesized material on nickel substrate was taken from reaction media, washed, dried, and then the product calcination was done at 400 °C for 2 h in air with 3 °C min^{-1} heating rate. .

2.2. Characterizations. The crystallographic data of the samples was investigated through Synchrotron X-ray diffraction [(SXRD, BL01C2 beamline at NSRRC, Taiwan), supported with Mar345 imaging plate and X-ray wavelength of 0.77491 Å X-ray, and then transferred to λ = 1.54178 Å X-ray by WinPLOTR software]. Their morphologies, structures and compositional investigations were examined by FESEM (JEOL JSM-6700F, with EDS instruments), TEM) and HRTEM (JEOL, JEM-2100F).

Surface analysis of samples was investigated using X-ray photo-electron spectroscopy (PHI Quantera) under Al Kα radiation (λ = 8.3406 Å). Co K-edge XANES spectra were examined at BL01C1 beamline of the NSRRC.

2.3. Electrochemical Measurements. For electrochemical measurements, the mass of active material was calculated by subtracting the mass of Ni foam sample before and after FCO-NFs growth. For confirmation, the pristine Ni substrate, without FCO-NFs growth, was cleaned, underwent hydrothermal reaction (without iron and cobalt precursors), heat-treated under the same experimental conditions, and weighted to ensure the correct mounted FCO-NFs grown mass. The mass loadings of the actual samples for lithium-ion battery and supercapacitor tests were 1.9 ± 0.3 mg cm^{-2}.

2.3.1. Li-ion Battery Measurement. Electrochemical experiments were carried out under room temperature with two-electrode coin cells (CR 2032), with lithium foil as both counter and reference electrode. A nickel foam piece mounted by FCO-NFs was directly utilized as the working electrode without addition of any polymeric binder or conductive materials. A glass fiber (18 mm in diameter, Pall Corporation) was employed as separator. Afterward, 1 M $LiPF_6$ in ethylene carbonate and dimethyl carbonate (1:1 by volume) was used as the electrolyte. The cell assembly was carried out in an argon-filled glovebox with both moisture and oxygen content below 1 ppm. Galvanostatic charge−discharge was carried out using a battery tester (AcuTech Systems Co., Ltd., Taiwan) with a voltage window of 0.01 to 3.0 V at a current density of 200 mA g^{-1}. Cyclic voltammetry (CV) test was conducted in the potential window of 0.01 to 3.0 V at a scan rate of 0.3 mV s^{-1} using an electrochemical workstation (AUTOLAB PGST30, Eco Chemie).

2.3.2. Supercapacitor Measurement. The electrochemical per-formance of the prepared FCO-NFs/Ni foam electrode for symmetric SC was investigated using two-electrode coin-type cells (CR 2032) assembled in an argon-filled glovebox. A pair of electrodes was assembled with a glass fiber separator with 1 M $LiClO_4$ in propylene carbonate organic electrolyte. The electrochemical properties of the SC were studied using cyclic voltammetry (CV), galvanostatic charge−discharge, and electrochemical impedance spectroscopy (EIS) using 760D (CH Instruments). The CV tests were carried out in the potential range of 0 to 2.5 V at different scan rates ranging from 1 mV s^{-1} to 5 V s^{-1}. The chrono charge−discharge measurements were also conducted at various current densities (0.1 to 20 A g^{-1}) in potential range of 0−2.5 V. The EIS measurements were performed in the frequency range of 1 MHz to 1 Hz (amplitude of 5 mV). The EIS data were analyzed using Nyquist plots. The specific capacitance (C, F g^{-1}) was then calculated from the CV curves according to the equation $C = i/m \Delta V$, where m (g) is the mass of active materials, ΔV (V s^{-1}) is the potential sweep rate, and i (A) is the current response obtained through integrating the area of the CV curve.[21] Energy density (E_d) and power density (P_d) were calculated from the capacitance (C) value obtained by cyclic voltamatry according to these equations:[22,23]

energy density

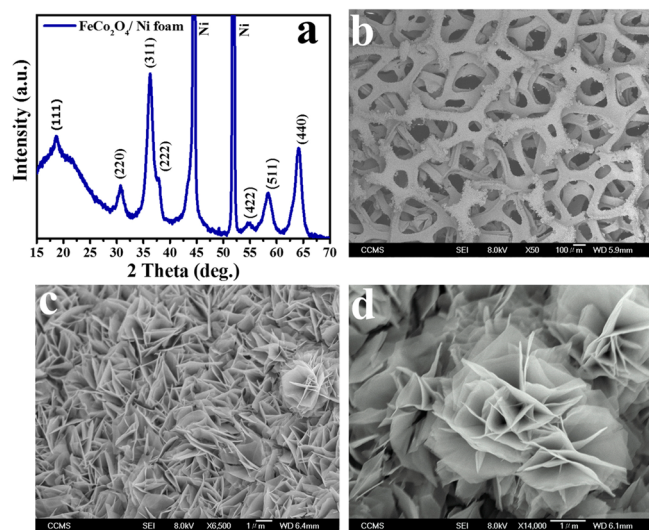$$E_d \ (\mathrm{W \, h \, K \, g^{-1}}) = 1/8 CV^2$$

power density

$$P_d \ (\mathrm{W \, K \, g^{-1}}) = E \Delta V / V \ (\mathrm{V = voltage \ window})$$

3. RESULTS AND DISCUSSION

3.1. FCO-NFs Characterazation. The X-ray diffraction (XRD) pattern of FCO-NFs developed on nickel foam after heat treatment at 400 °C for 2 h is presented Figure 1a.

Figure 1. (a) XRD pattern and (b−d) typical FE-SEM images at different magnifications of FCO-NFs on nickel foam after calcination at 400 °C for 2 h in air.

Excluding the two peaks resulting from metallic Ni at approximately 2θ of 44.5° and 51.9° (JCPDS 04-0850), whole diffraction peaks could be apparently indexed to $FeCo_2O_4$ spinel phase ($Fd3m$ space group); they demonstrate good agreement with the reported values in prior reports.[17,18,24] No further peaks, related to NiO, MnO_2, or CoO, are detected in the produced material, indicating the uniform growth of $FeCo_2O_4$ on the surface of nickel substrate. The morphology of FCO_NFs grown on nickel foam was investigated by field emission scan electron microscopy (FE-SEM). Figures 1b−d show the characteristic morphology of the FCO-NFs on nickel foam. As shown, the nanoflakes are homogeneously grown on nickel foam, developing a uniform coating on the surface (Figure 1b) and forming an enlarged petal-like nanoflake structure. These features are connected to one another, and this formation results in a cross-linked structure that might possess high mechanical strength. Further information on the FCO-NFs microstructure can be attained from the transmission electron microscopy (TEM) images in Figure 2. The image of low magnification (Figure 2a) implies that the nanoflakes are incessant. They have a coarse surface in which the interconnected nanoparticles form sheet-like structures. The magnified image (Figure 2c) clearly shows that pores are distributed throughout the surface of the nanoflakes. The formation of the pores in the nanoflakes could be related to the liberation of gases during thermal treatment during the decomposition of the precursors.[25] The resolved lattice fringes shown in Figure 2c are about 0.24 and 0.47 nm, which could be
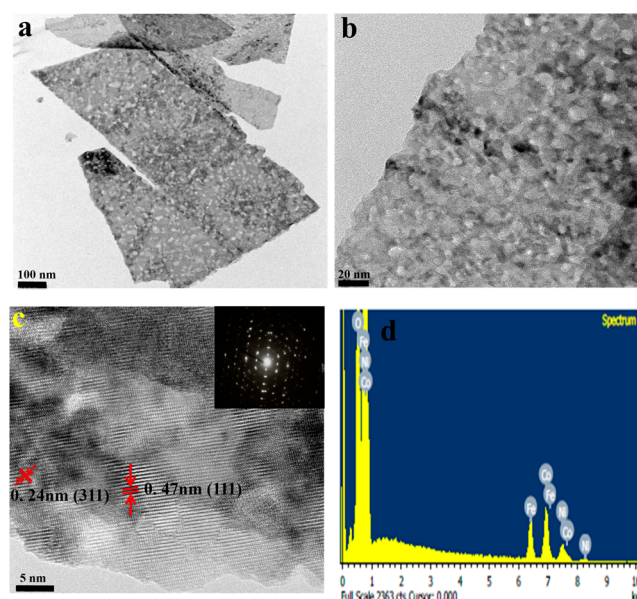
Figure 2. TEM and HRTEM analysis of the FCO-NFs detached from nickel foam: (a) morphology at low magnification, (b) morphology at high magnification (noticing of the porous features), (c) HRTEM image with the corresponding SAED pattern (inset), and (d) EDS microanalysis of FCO-NFs on Ni foam.

assigned to the (311) and (111) planes of the $FeCo_2O_4$ cubic phase. This result further confirms the formation of crystalline FCO-NFs, and has a consistency with the XRD pattern. Moreover, the corresponding selected area electron diffraction (SAED) pattern (Figure 2c inset) indicates the single-crystalline character of the nanoflakes, Energy-dispersive X-ray spectrometry (EDS) microanalysis of the NFs (Figure 2d) displays that the nanoflakes comprises only Fe, Co, and O elements with atomic ratio of almost of 1:2:4, indicating the formation of pure $FeCo_2O_4$.

The chemical composition and the purity of the FCO-Nfs product were investigated using X-ray photoelectron spectroscopy (XPS). Figure 3a elucidates the XPS spectra of Fe $2p$. The peak deconvolution and fittings were carried out using Gaussian−Lorentzian shaped peaks based on the Shirley background correction. Two peaks are observed at 709.5 and 722.6 eV, consistent with spin−orbit peaks of the Fe $2p_{3/2}$ and Fe $2p_{1/2}$, in addition to the presence of a "shoulder" satellite peak at 714.6 eV. These results indicate the presence of Fe^{2+}.[26] As can be seen in Figure 3b, the Co $2p$ pattern demonstrates two peaks at 779.2 (main peak, Co^{3+}) and 785.1 eV (satellite peak, Co^{2+}), that could be ascribed to Co $2p_{3/2}$ and its satellite peak. Another peaks are detected at 794.6 (main peaks, Co^{3+}) and 801.7 eV (satellite peak, Co^{2+}/Co^{3+}) that could be ascribed to Co $2p_{1/2}$ and its satellite peak.[18] From the binding energies of Co $2p$ main lines and the splitting due to the spin−orbit coupling, besides the energy gaps separating the main lines and satellite peaks, it can be said that Co(II) and Co(III) cations together are exist. The O $1s$ XPS spectrum (Figure 3c) displays two strong main peaks at about 529.6 eV (corresponding to a characteristic bond between metal and oxygen) and at 531.1 eV which is corresponding to the OH^- groups oxygen, revealing of hydroxylation of the material surface. The X-ray absorption near edge structure (XANES) spectrum shown in Figure 3d and its inset (Co K-edge and per edge region) show that $FeCo_2O_4$ is close to Co_3O_4 mixed valence (Co^{2+} and Co^{3+}),
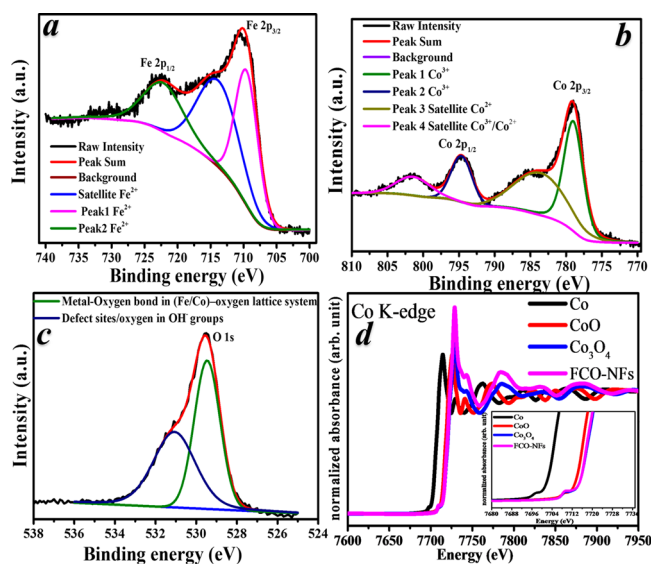
Figure 3. XPS and XANES spectra for the FCO-NFS detached from nickel foam: (a) Fe 2p XPS, (b) Co 2p XPS, (c) O 1s XPS, and (d) Co K-edge XANES and pre-edge region (inset).

indicating the coexistence of both Co^{2+} and Co^{3+} cations in $FeCo_2O_4$. This result is consistent with that of the XPS spectra.
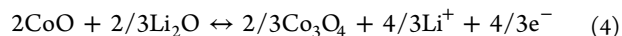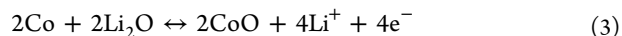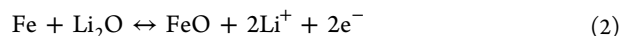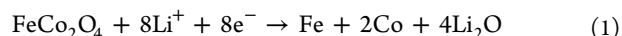
3.2. FCO-NFs Electrochemical Performance. The electrochemical performance of the FCO-NFs grown on nickel foam is estimated as conductive agent and binder-free electrode for LIBs and SCs. For LIB anode, the electrochemical properties of FCO-NFs electrode was first investigated through cyclic voltammetry (CV) to discern the charge and discharge reaction potentials. Figure 4a displays the initially three CV
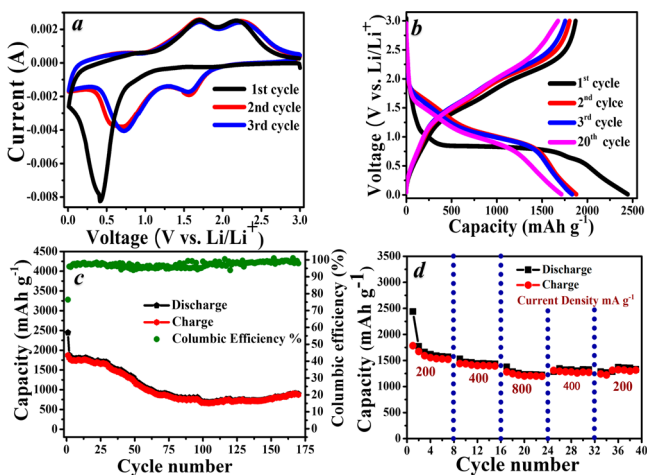
Figure 4. Electrochemical performance of FCO-NFs electrode for LIBs: (a) CVs of the first three cycles at 0.3 mV s^{-1} scan rate and voltage of 0.01 to 3.0 V; (b) discharge/charge profiles for the selected cycles (at 200 mA g^{-1}); (c) cycle performance at 200 mA g^{-1}; and (d) rate capability test at different current densities.

curves of FCO-NFs on nickel foam electrode obtained at 0.3 mV s^{-1} scan rate and potential range of 0.01−3.0 V. The voltammogram for the first cycle is noticeably different among these ones of the subsequent cycles, and no considerable variation is noticed between the second and third cycles. In the first cycle, a single intense reduction current peak is detected at 0.42 V in the cathodic scan. This peak could be ascribed to Li

intercalation into the crystal structure after that $FeCo_2O_4$ crystal lattice destructed (amorphous phase formation) and development of the corresponding metal nanoparticles[4] (reduction of Co^{3+} to Co^{2+}, Co^{2+} to metallic Co, and Fe^{2+} to metallic Fe in $FeCo_2O_4$ crystals). In addition to these processes is the forming of amorphous Li_2O, along with growing of solid electrolyte interphase (SEI) layer as a result of the disintegration of electrolyte.[8,18,27] The cathodic irreversible peak could be explicated by eq 1. The first-charge sweep shows a doublet peak at potentials ∼1.69 and ∼2.2 V, which is ascribed to the oxidation of Co to Co^{2+} and Co^{3+} and of Fe to Fe^{2+}. The reduction peaks in the second and third cycles move to 0.72 and 1.57 V, differing significantly from that electrochemical reaction occurred irreversibly in the first cycle during discharge. These peaks are induced by the reduction reactions of FeO, CoO, and Co_3O_4 to Fe and Co metals. In the consecutive cycles, two reversible anodic peaks are observable at 1.68 and 2.25 V, which could be ascribed to the oxidation of Fe^0 to Fe^{2+} and of Co^0 to Co^{2+}/Co^{3+}, respectively, indicating that reversible oxidation−reduction processes take place in the charge−discharge cycles. Based on the displacive redox mechanism, these processes could be described by eqs 2 to 4.[18,27]

$$FeCo_2O_4 + 8Li^+ + 8e^- \rightarrow Fe + 2Co + 4Li_2O \tag{1}$$

$$Fe + Li_2O \leftrightarrow FeO + 2Li^+ + 2e^- \tag{2}$$

$$2Co + 2Li_2O \leftrightarrow 2CoO + 4Li^+ + 4e^- \tag{3}$$

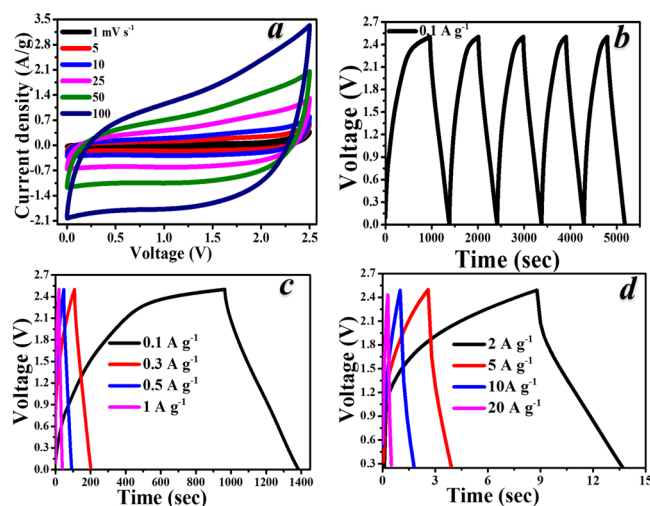$$2CoO + 2/3Li_2O \leftrightarrow 2/3Co_3O_4 + 4/3Li^+ + 4/3e^- \tag{4}$$

Thereafter The FCO-NFs were evaluated as anode for LIBs, representative charge−discharge characters of the 1st, 2nd, 3rd, and 20th cycles at current density of 200 mA g^{-1} are presented in Figure 4b. This electrode exhibits first discharge and charge capacities of 2445 and 1870 mAh g^{-1}, respectively, corresponding to 76.5% of the first Coulombic efficiency. The high discharge capacity of first cycle might as well be correlated to the Li$^+$ diffusion distance shortening alongside increasing the number of diffused ions as a result of the porous structure of 2D NF's arrays, besides to the influence of the partly reversible formation−decomposition of the SEI and formation of gel polymeric layer resulted from electrolyte dissolution.[18,28] The plateau of first discharge cycle exists at ∼0.89 V, corresponding intercalating of Li ion into the $FeCo_2O_4$ crystal system, at which the crystal lattice turns to amorphous constitution followed by the formation of the metallic nanoparticles through a two-phase reaction formation. Accordingly, the charging operation (extraction of Li from Fe−Co−Li_2O composite) will not result in the reformation of the spinel structure, but only the individual oxides, FeO or CoO (Co_3O_4), are formed. Enabling the realization of larger reversible capacity and giving stable and near theoretical capacities on long-term cycling of the $FeCo_2O_4$ by conversion reaction,[4] which are coherent with the CV performance. In the following cycles, the plateau at 0.89 V shifts from 1.2 to 1.3 V, indicating that the irreversible reactions occurred throughout the first cycle. The findings also confirm that different electrochemical reactions regulate the following cycles. The second, third, and 20th cycles' discharge capacities of the electrode are 1877, 1831, and 1713 mA g^{-1}, respectively, demonstrating the great stability of the electrode material. The loss in capacity (irreversibility) in the first cycle (23.2%) could be ascribed to the SEI forming and reduction of metal oxides to

its corresponding metal atoms beside Li_2O formation, that is usually noticed in several electrode materials.[29] Figure 4c displays the charge–discharge capacity of the FCO-NFs electrode versus the cycles number at cycling current density of 200 mA g^{-1}. Within 170 cycles, the capacity fades up to 70 cycles. Thereafter, the reversible capacities stabilize and slightly increase gradually up to 170 cycles (~905 mAh g^{-1} for cycle 170 discharge capacity) with a significant improvement in Coulombic efficiency. The obtained Coulombic efficiency implies that the charge–discharge process steadily steadies. To investigate the performance rate of the FCO-NFs, the rate capabilities were investigated using multiple-step charging/ discharging at several current densities (200 to 800 mA g^{-1}). Figure 4d shows that the cell has good rate capability with average discharge capacities of 1570, 1433, and 1222 mA h g^{-1}, once the current density raised from 200 to 400 and 800 mA g^{-1}, respectively. By varying the current density back to 400 and 200 mA g^{-1}, an average discharge capacity as high as 1324 and 1330 mAh g^{-1} could be recovered. These results show that the FCO-NFs anode for LIB has significantly high cycling performance, capacity retention and rate capability.

The electrochemical performance of the FCO-NFs on nickel foam is also evaluated for application as electrodes for SCs. To confirm the effectiveness of the material for charge storing, testing of electrochemical capacitance was examined through cyclic voltammetry (CV) and the charge–discharge technique in a symmetrical two electrode system containing FCO-NFs on nickel foam electrodes and 1 M $LiClO_4$/PC nonaqueous electrolyte at potential window of 0 to 2.5 V. The CV curves found by varying the scan rate from 1 to 100 mV s^{-1} are shown in Figure 5a. The CV curves are deviated rectangular-like
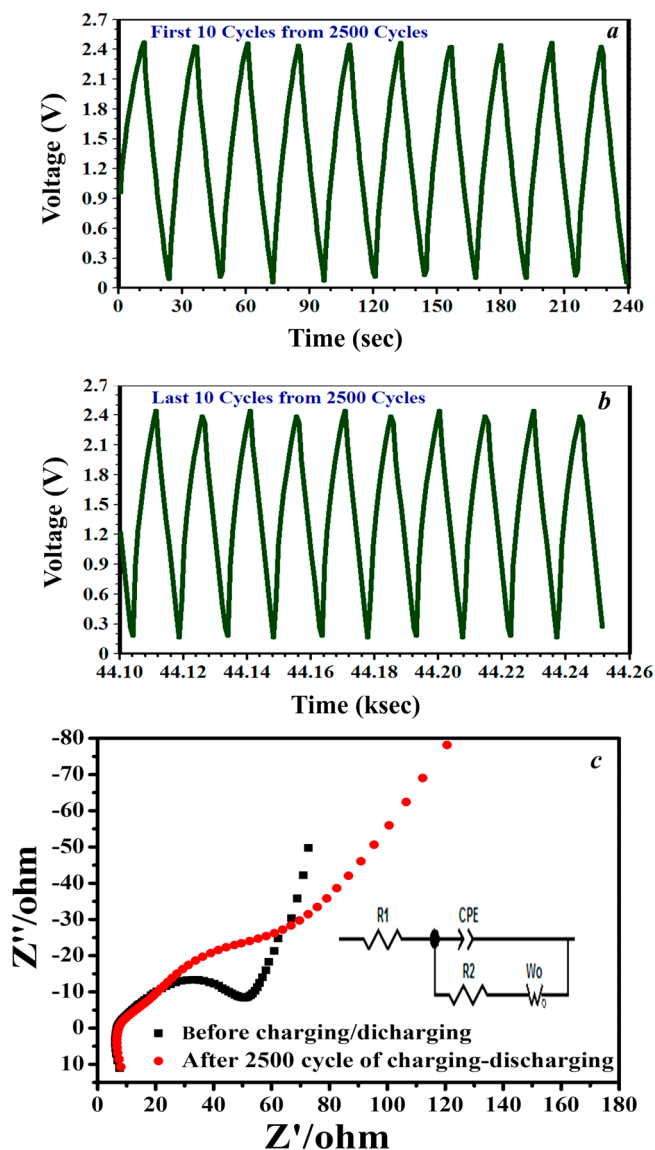

Figure 5. Electrochemical performance of FCO-NFs electrode for symmetric SCs: (a) CV responses at different scan rates of 1−100 mV s^{-1}; (b) charge−discharge curves of the first 5 cycles of the SCs at 0.1 A g^{-1}; (c and d) symmetric SC's first cycle behavior at different current densities.

instead, that could be attributed to the electrode inherent resistance. This resistance can be ascribed to intensified polarization, fast transfer of charges, and diffusion of captions. The CV testing of the electrode under high sweep rates of 0.5, 1, and 5 V s^{-1} suggests potential use of such material in SCs used in high-power applications. The symmetric cell made from FCO-NFs on nickel foam electrode shows high specific capacitances of 433, 225, 184, 150.8, 129.2, 109.6, 65.1, and 46.6 F g^{-1} at scan rates of 1, 5, 10, 25, 50, 100, 500, and 1000 mV s^{-1}, respectively (Table S1, Supporting Information). Additionally, cycling at high scan rate of 5000 mV s^{-1}, capacitive performance can even be detected with a 16.7 F g^{-1} specific capacitance. For additional estimation of the electrochemical performance of the FCO-NFs on nickel foam electrode, chrono charge–discharge tests were done at various current densities. Electrode Charge–discharge performance is crucial in the examination and estimation of the performance of the active material under real operational circumstances.[19] The constant current charge–discharge curves for the SC electrodes at 0.1 A g^{-1} in the potential range of 0−2.5 V are shown in Figure 5b (first five cycles; see also Figure S2, Supporting Information). Through the charge–discharge processes, the curve of charging step is not quite symmetrical with its related discharging step, showing a small decline in internal resistance (IR drop) and indicating pseudocapacitive behavior. The anodic charging segment is consistent with cathodic discharging segment with nearly triangular shape-like curve in the chrono charge–discharge performance as shown in Figure S2, Supporting Information, (except for the first 2 cycles in 0.1 A g^{-1} because of internal resistance at low charging current density, Figure 5b), which is suggestive of a highly reversible charge–discharge reaction or a very good reversible capacitive material. These results indicate that the cell potential is linearly changed with time, signifying the pseudocapacitive character of the electrode obtaining from storage of charges through adsorption–desorption at the electrode–electrolyte interface, in addition to double-layer contributions and probable Li$^+$ insertion/extraction mechanism between the electrode and the $LiClO_4$/PC electrolyte.[31] Figures 5c and d shows the charge–discharge curves of different characteristic current cycling rates (0.1, 0.3, 0.5, 1, 5, 10, 15, and 20 A g^{-1}). Whole curves exhibit symmetrical characters of the charging and discharging counterparts, suggesting the perfect pseudocapacitive character of rapid charge/discharge processes.[30]

The cycle performances are important for electrochemical SCs. The electrode durable stability was studied by chrono charge–discharge technique at current density of 2 A g^{-1} in the potential ranging between 0 and 2.5 V for 2500 cycles. The first and the last 10 charge–discharge curves are showed in Figures 6a and b, which display nearly the same shape, revealing outstanding long-term stability of the electrode even under rapid charge–discharge situations. Supporting Information Figure S3a shows the plots of Coulombic efficiency vs cycle's number. Coulombic efficiency is calculated by dividing the discharge current on charging current (t_d/t_c of the 2500 cycles at current density of 2 A g^{-1}). The Coulombic efficiency is close to 100%, indicating the stability of and symmetry of the electrode under long-cycling test.

The energy density and power density of the supercapacitor are calculated from CV using the equation given in the Experimental Section and the typical Ragone plot is shown in S3b, Supporting Information. The values of energy densities and the power densities are shown in Table S1, Supporting

character and exhibit nearly perfect capacitive performances at sweep rates up to 100 mV s^{-1} (Figure S1, Supporting Information), indicating the rapid current response to voltage reversal (small contact resistance) and reveals the pseudocapacitive behavior of the electrodes.[30] The CV curves differ from that rectangular nature at higher scan rates (500−5000 mV s^{-1}, Figure S1, Supporting Information) and exhibit an ovoid shape

Figure 6. (a and b) First and last 10 charge−discharge curves at 2 A g^{-1} current density in the potential range between 0 and 2.5 V for 2500 cycles, and (c) Nyquist plot recorded for symmetrical SC cells containing FCO-NF/Ni foam before and after cycling to 2500 cycles (inset shows equivalent circuit of the FCO-NFs/Ni foam-based symmetric SC).

Information. The energy density of FCO-NFs electrode at scan rate of 1 mV s^{-1} can approach 93.9 Wh kg^{-1} at a power of 135.3 W kg^{-1}. A strong drop in the energy density with increasing the power densities can also be observed by increasing the scan rate. Even at a high power density of 26093.7 W kg^{-1}, the energy density still can be kept at approximately 3.6 Wh kg^{-1} (at scan rate of 5 V s^{-1}), which reveals a large power range that can be achieved with maintaining a suitable energy density.

To further quantitatively examine the interfacial electro-chemical behavior of the SC electrode−electrolyte interface, electrochemical impedance spectroscopy (EIS) measurements were conducted before and after the galvanostatic charging−discharging test. Figure 6c displays the Nyquist plots of symmetrical SC cells which fabricated based on FCO-NFs on nickel foam electrodes before and after 2500 charge−discharge cycling. The Nyquist plot mainly consists on a semicircular

section above the real axis, and then a straight line in the low-frequency section. The line at lower frequencies is nearly straight, indicating the diffusion-controlled process with prominent capacitive performances with a tiny resistance for diffusion.[8,32] The semicircle intercept at high frequency on the plot real axis (Z') reflects a joined resistance, that contains the inherent electrode resistance, electrolyte resistance, and contact resistance. The semicircle radius relates to the Faradaic charge transfer resistance and EDLC at the electrode−electrolyte interface.[32] At the low-frequency area, the linear part is associated with resistance (Warburg resistance W_o) of electrolyte and ionic diffusion/transport into the electrode surface. The diffusion line is nearly perpendicular to the real axis in the impedance imaginary portion at the low-frequency section, representing the ionic diffusion swift in the electrolyte and adsorption on the electrode surface, suggesting the ideal capacitive performance of the electrodes.[33] The inset of Figure 6 illustrates the symmetrical SC equivalent circuit, in that equivalent circuit, R_1 is connected in series to a capacitance of the double-layer (CFE, a CPE is often used in a model rather than a capacitor to compensate for nonhomogeneity in the system), which is connected in parallel to R_2 and W_o. By fitting the experimental data using ZviewTM software (Figure S4, Supporting Information), R_s values of 7.6 and 8 Ω and R_{ct} values of 47.5 and 52 Ω can be obtained from the electrode before and after 2500 cycles of charging/discharging experiments. The values of R_1 are almost the same, whereas the values of R_2 vary insignificantly. A minimal slope differences is observed from the vertical diffusion lines, indicating the excellent capacitive performance of the electrode before and after long-term charging/discharging.

The high capacitive performance might be ascribed to the nanoflakes 2D structure that eases rapid transport of electrons between the active materials and the charge collecting substrate. The nanoflakes could act as 2D transport routes for storage and transfer of the electrical charges from/to the electrodes. In addition, the nanoflakes have large specific surface areas and porous features which could enlarge the efficient liquid/solid interfacial area, resulting in effective use of the active material by increasing the number of electroactive sites. Therefore, FCO-NFs supported on flexible conductive nickel foam can directly serve as free conductive agents and binder electrodes for energy storage systems such as LIBs and symmetric SCs.

4. CONCLUSIONS

Interconnected FCO-NFS were productively developed on nickel foam substrates through a facile hydrothermal method accompanied by the calcination at 400 °C in air. The LIB anode fabricated from the FCO- NFs on nickel foam exhibits a first discharge capacity as high as 2445 mAh g^{-1} at 200 mA g^{-1} current density. This LIB anode also shows significant long-term cycling and rate capabilities performance. The symmetric SC assembled from FCO-NFs on nickel foam electrode exhibits electrochemical capacitance as high as 433 and 225 F g^{-1} at scan rates of 1 and 5 mV s^{-1}, respectively. This symmetric SC electrode also shows capacitance activities under high scan rates of 1000 and 5000 mV s^{-1}. Such highly integrated binder- and additive-free electrodes made by direct growth of electroactive FCO-NFS on conductive substrates have a great potential for the assembly of high rendering energy storage devices.

■ AUTHOR INFORMATION

Corresponding Authors

*Tel.: +886-2-77346088. E-mail: sfhu.hu@gmail.com.

*E-mail: rsliu@ntu.edu.tw. Tel.: +886-2-33661169. Fax: +886-2-3366 8671.

Notes

The authors declare no competing financial interest.

■ REFERENCES

(1) Yuan, C.; Wu, H. B.; Xie, Y.; Lou, X. W. Mixed Transition-Metal Oxides: Design, Synthesis, and Energy-Related Applications. *Angew. Chem., Int. Ed.* **2014**, *53*, 1488−1504.

(2) Jiang, J.; Li, Y.; Liu, J.; Huang, X.; Yuan, C.; Lou, X. W. Recent Advances in Metal Oxide-Based Electrode Architecture Design for Electrochemical Energy Storage. *Adv. Mater.* **2012**, *24*, 5166−5180.

(3) Arico, A. S.; Bruce, P.; Scrosati, B.; Tarascon, J.-M.; van Schalkwijk, W. Nanostructured Materials for Advanced Energy Conversion and Storage Devices. *Nat. Mater.* **2005**, *4*, 366−377.

(4) Reddy, M. V.; Subba Rao, G. V.; Chowdari, B. V. R. Metal Oxides and Oxysalts as Anode Materials for Li Ion Batteries. *Chem. Rev.* **2013**, *113*, 5364−5457.

(5) Simon, P.; Gogotsi, Y. Materials for Electrochemical Capacitors. *Nat. Mater.* **2008**, *7*, 845−854.

(6) Gao, G.; Wu, H. B.; Lou, X. W. D. Citrate-Assisted Growth of $NiCo_2O_4$ Nanosheets on Reduced Graphene Oxide for Highly Reversible Lithium Storage. *Adv. Energy Mater.* **2014**, DOI: 10.1002/aenm.201400422.

(7) Liu, L.; Yang, Y. Shape-Controlled Synthesis of MnCo Complex Oxide Nanostructures Via a Polyol-Based Precursor Route and Their Catalytic Properties. *Superlattices Microstruct.* **2013**, *54*, 26−38.

(8) Mohamed, S. G.; Hung, T.-F.; Chen, C.-J.; Chen, C. K.; Hu, S.-F.; Liu, R.-S. Efficient Energy Storage Capabilities Promoted by Hierarchical $MnCo_2O_4$ Nanowire-Based Architectures. *RSC Adv.* **2014**, *4*, 17230−17235.

(9) Li, L.; Zhang, Y. Q.; Liu, X. Y.; Shi, S. J.; Zhao, X. Y.; Zhang, H.; Ge, X.; Cai, G. F.; Gu, C. D.; Wang, X. L.; Tu, J. P. One-Dimension $MnCo_2O_4$ Nanowire Arrays for Electrochemical Energy Storage. *Electrochim. Acta* **2014**, *116*, 467−474.

(10) Yuan, C.; Li, J.; Hou, L.; Zhang, X.; Shen, L.; Lou, X. W. Ultrathin Mesoporous $NiCo_2O_4$ Nanosheets Supported on Ni Foam as Advanced Electrodes for Supercapacitors. *Adv. Funct. Mater.* **2012**, *22*, 4592−4597.

(11) Li, J.; Xiong, S.; Liu, Y.; Ju, Z.; Qian, Y. High Electrochemical Performance of Monodisperse $NiCo_2O_4$ Mesoporous Microspheres as an Anode Material for Li-Ion Batteries. *ACS Appl. Mater. Interfaces* **2013**, *5*, 981−988.

(12) Liu, B.; Liu, B.; Wang, Q.; Wang, X.; Xiang, Q.; Chen, D.; Shen, G. New Energy Storage Option: Toward $ZnCo_2O_4$ Nanorods/Nickel Foam Architectures for High-Performance Supercapacitors. *ACS Appl. Mater. Interfaces* **2013**, *5*, 10011−10017.

(13) Bai, J.; Li, X.; Liu, G.; Qian, Y.; Xiong, S. Unusual Formation of $ZnCo_2O_4$ 3D Hierarchical Twin Microspheres as a High-Rate and Ultralong-Life Lithium-Ion Battery Anode Material. *Adv. Funct. Mater.* **2014**, *24*, 3012−3020.

(14) Kang, W.; Tang, Y.; Li, W.; Li, Z.; Yang, X.; Xu, J.; Lee, C.-S. Porous $CuCo_2O_4$ Nanocubes Wrapped by Reduced Graphene Oxide as High-Performance Lithium-Ion Battery Anodes. *Nanoscale* **2014**, *6*, 6551−6556.

(15) Butt, F. K.; Cao, C.; Ahmed, R.; Khan, W. S.; Cao, T.; Bidin, N.; Li, P.; Wan, Q.; Qu, X.; Tahir, M.; Idrees, F. Synthesis of Novel ZnV_2O_4 Spinel Oxide Nanosheets and Their Hydrogen Storage Properties. *CrystEngComm* **2014**, *16*, 894−899.

(16) Zhu, Y.; Cao, C.; Tao, S.; Chu, W.; Wu, Z.; Li, Y. Ultrathin Nickel Hydroxide and Oxide Nanosheets: Synthesis, Characterizations and Excellent Supercapacitor Performances. *Sci. Rep.* **2014**, DOI: 10.1038/srep05787.

(17) Laouini, E.; Berghoute, Y.; Douch, J.; Mendonça, M. H.; Hamdani, M.; Pereira, M. I. S. Electrochemical Behaviour of $Fe_xCo_{3−x}O_4$ with (x = 0, 1, 2 and 3) Oxides Thin Film Electrodes in Alkaline Medium. *J. Appl. Electrochem.* **2009**, *39*, 2469−2479.

(18) Sharma, Y.; Sharma, N.; Subba Rao, G. V.; Chowdari, B. V. R. Studies on Spinel Cobaltites, $FeCo_2O_4$ and $MgCo_2O_4$ as Anodes for Li-Ion Batteries. *Solid State Ionics* **2008**, *179*, 587−597.

(19) Rakhi, R. B.; Chen, W.; Cha, D.; Alshareef, H. N. Nanostructured Ternary Electrodes for Energy-Storage Applications. *Adv. Energy Mater.* **2012**, *2*, 381−389.

(20) Stoller, M. D.; Ruoff, R. S. Best Practice Methods for Determining an Electrode Material's Performance for Ultracapacitors. *Energy Environ. Sci.* **2010**, *3*, 1294−1301.

(21) Yuan, C.-Z.; Gao, B.; Zhang, X.-G. Electrochemical Capacitance of $NiO/Ru_{0.35}V_{0.65}O_2$ Asymmetric Electrochemical Capacitor. *J. Power Sources* **2007**, *173*, 606−612.

(22) Jang, J. H.; Kato, A.; Machida, K.; Naoi, K. Supercapacitor Performance of Hydrous Ruthenium Oxide Electrodes Prepared by Electrophoretic Deposition. *J. Electrochem. Soc.* **2006**, *153*, A321−A328.

(23) Anothumakkool, B.; Bhange, S. N.; Unni, S. M.; Kurungot, S. 1-Dimensional Confinement of Porous Polyethylenedioxythiophene Using Carbon Nanofibers as a Solid Template: an Efficient Charge Storage Material with Improved Capacitance Retention and Cycle Stability. *RSC Adv.* **2013**, *3*, 11877−11887.

(24) Ferreira, T. A. S.; Waerenborgh, J. C.; Mendonça, M. H. R. M.; Nunes, M. R.; Costa, F. M. Structural and Morphological Characterization of $FeCo_2O_4$ and $CoFe_2O_4$ Spinels Prepared by a Coprecipitation Method. *Solid State Sci.* **2003**, *5*, 383−392.

(25) Hu, L.; Zhong, H.; Zheng, X.; Huang, Y.; Zhang, P.; Chen, Q. $CoMn_2O_4$ Spinel Hierarchical Microspheres Assembled with Porous Nanosheets as Stable Anodes for Lithium-Ion Batteries. *Sci. Rep* **2012**, *2*, 986−993.

(26) Yamashita, T.; Hayes, P. Analysis of XPS Spectra of Fe^{2+} and Fe^{3+} Ions in Oxide Materials. *Appl. Surf. Sci.* **2008**, *254*, 2441−2449.

(27) Li, S.; Wang, B.; Liu, J.; Yu, M. In Situ One-Step Synthesis of $CoFe_2O_4$/Graphene Nanocomposites as High-Performance Anode for Lithium-Ion Batteries. *Electrochim. Acta* **2014**, *129*, 33−39.

(28) Li, J.; Xiong, S.; Li, X.; Qian, Y. A Facile Route to Synthesize Multiporous $MnCo_2O_4$ and $CoMn_2O_4$ Spinel Quasi-Hollow Spheres with Improved Lithium Storage Properties. *Nanoscale* **2013**, *5*, 2045−2054.

(29) Liu, B.; Zhang, J.; Wang, X.; Chen, G.; Chen, D.; Zhou, C.; Shen, G. Hierarchical Three-Dimensional $ZnCo_2O_4$ Nanowire Arrays/Carbon Cloth Anodes for a Novel Class of High-Performance Flexible Lithium-Ion Batteries. *Nano Lett.* **2012**, *12*, 3005−3011.

(30) Wang, T.; Peng, Z.; Wang, Y.; Tang, J.; Zheng, G. MnO Nanoparticle@Mesoporous Carbon Composites Grown on Conducting Substrates Featuring High-Performance Lithium-Ion Battery, Supercapacitor and Sensor. *Sci. Rep* **2013**, *3*, 2693−2701.

(31) Kalubarme, R. S.; Jadhav, H. S.; Park, C.-J. Electrochemical Characteristics of Two-Dimensional Nano-Structured MnO_2 for Symmetric Supercapacitor. *Electrochim. Acta* **2013**, *87*, 457−465.

(32) Wang, J.-G.; Yang, Y.; Huang, Z.-H.; Kang, F. A High-Performance Asymmetric Supercapacitor Based on Carbon and Carbon−MnO_2 Nanofiber Electrodes. *Carbon* **2013**, *61*, 190−199.

(33) Ramchandra, S. K.; Yong-Han, K.; Chan-Jin, P. One Step Hydrothermal Synthesis of a Carbon Nanotube/Cerium Oxide Nanocomposite and Its Electrochemical Properties. *Nanotechnology* **2013**, *24*, No. 365401.

22708

dx.doi.org/10.1021/am5068244 | *ACS Appl. Mater. Interfaces* 2014, 6, 22701−22708